Atmos. Meas. Tech. Discuss., 7, 1603–1644, 2014
www.atmos-meas-tech-discuss.net/7/1603/2014/
doi:10.5194/amtd-7-1603-2014

Atmospheric Measurement Techniques Discussions

Hydrometor classification from 2 dimensional videodisdrometer data

J. Grazioli[1], D. Tuia[2], S. Monhart[3], M. Schneebeli[3], T. Raupach[1], and A. Berne[1]

[1]Environmental Remote Sensing Laboratory (LTE), École Polytechnique Fédérale de Lausanne (EPFL), Lausanne, Switzerland
[2]Laboratory of Geographic Information Systems (LASIG), École Polytechnique Fédérale de Lausanne (EPFL), Lausanne, Switzerland
[3]Federal Office of Meteorology and Climatology, Meteo Swiss, Locarno-Monti, Switzerland

Received: 19 December 2013 – Accepted: 4 February 2014 – Published: 17 February 2014

Correspondence to: A. Berne (alexis.berne@epfl.ch)

Published by Copernicus Publications on behalf of the European Geosciences Union.

Abstract

This paper presents a hydrometeor classification technique based on two-dimensional video disdrometer (2DVD) data. The method provides an estimate of the dominant hydrometeor type falling over time intervals of 60 s during precipitation, using as input the statistical behavior of a set of particle descriptors, calculated for each particle image. The employed supervised algorithm is a support vector machine (SVM), trained over precipitation time steps labeled by visual inspection. In this way, 8 dominant hydrometeor classes could be discriminated. The algorithm achieves accurate classification performances, with median overall accuracies (Cohen's $\mathcal{K}$) of 90 % (0.88), and with accuracies higher than 84 % for each hydrometeor class.

1 Introduction

The two-dimensional video disdrometer (Kruger and Krajewski, 2002), 2DVD hereafter, significantly improved the use of ground observations to describe the microphysics and microstructure of precipitation both in the solid and the liquid phase. The system, based on simultaneous observations of falling objects with two orthogonally-oriented cameras, has been used to characterize the relationships linking raindrop shape, size and terminal velocity (e.g. Thurai and Bringi, 2005; Thurai et al., 2009). It has also been employed to compare rainfall observations on the ground with weather radar measurements (Schuur et al., 2001; Thurai et al., 2008; Cao et al., 2008; Zhang et al., 2008). Regarding snowfall, the 2DVD has been used to derive the statistical properties of particle size distributions of winter storms (Brandes et al., 2007), to improve the conversion of weather radar observations to equivalent liquid precipitation (Huang et al., 2010), and to simulate radar observations in agreement with the measured snowfall microstructure (Zhang et al., 2011).

In the present work we employ 2DVD measurements for the classification of hydrometeors, with a special focus on ice phase precipitation. The expression "hydrometeor

AMTD
7, 1603–1644, 2014

classification" refers to techniques that aim at retrieving the qualitative information about the dominant hydrometeor type characterizing the precipitation. Such information can then be used for risk assessment (hazardous hydrometeors identification), for parametrization and validation of numerical weather prediction (NWP) models (e.g., Xue et al., 2000), or to support microphysical investigations (e.g., Houze, 1993; Schneebeli et al., 2013). Hydrometeor classification techniques are nowadays implemented in different types of measurement sensors. Typical examples in remote sensing are the algorithms designed for ground based polarimetric weather radars (Straka et al., 2000; Dolan and Rutledge, 2009; Chandrasekar et al., 2013), or for airborne radars and lidars observing ice phase clouds (e.g., Delanoe et al., 2013). These sensors allow to sample large domains at high resolution in a short time lapse, but their classification retrievals are indirect, constrained by numerical simulations, and difficult to validate extensively. On the contrary, airborne particle probe imagers (e.g., Feind, 2008), allow to obtain a direct classification along the aircraft fly paths but only (given the high cost of these platforms) during very specific measurement campaigns. Ground-based instruments sample precipitation directly on site (even though on small sampling volumes), and could be used to classify hydrometeors, thus becoming a point reference for remote sensing retrievals. Only few research works have been devoted to the implementation of classification schemes for such instruments, and their focus was mostly on mixed-phase precipitation (Yuter et al., 2006), or in the exploration of the potential synergy between multiple sensors (Marzano et al., 2010). Some commercial disdrometers (i.e., PARSIVEL), orginally designed for rainfall studies, provide an estimation of the precipitation type associated with each measurent by making assumptions on fall velocity and and equivalent rainfall intensity. For this reason, they are prone to unreliable estimates in complex site conditions.

In this context the information provided by the 2DVD is of particular interest because a couple of two dimensional views, together with fall velocity, is provided for each particle. Such features alone allow expert users to interpret the images and visually recognize in them specific hydrometeor types (e.g., Zhang et al., 2011). This suggests

AMTD
7, 1603–1644, 2014

that automatic classification methods, based on training over visually interpreted (labelled) episodes may be well suited to perform hydrometeor classification. Supervised classification algorithms, as the support vector machine, (SVM, Boser et al., 1992) are nowadays used to face tasks of similar kind, as example for land cover classification (Camps-Valls and Bruzzone, 2005), wind power forecast (Foresti et al., 2011; Zeng and Qiao, 2011), and weather prediction (Sullivan, 2009). SVM is a linear and binary supervised classifier, that finds the optimal separations between observations belonging to different classes. These observations are defined by a set of numerical features and the optimal separation is learned from a training set where the association between input observation and output class is known. SVM is able to handle high dimensional inputs, is less prone to over-fitting issues than other supervised methods (Camps-Valls and Bruzzone, 2009), and it has been shown to be top ranked for weather prediction classification tasks (e.g., Elmore, 2010). Furthermore SVM allows to retrieve the most relevant input features driving the classification, and rank them in order of importance, with the implementation of multiple kernel learning (SVM-MKL) techniques (Rakotomamonjy et al., 2008; Tuia et al., 2010).

In this paper we train a SVM model on 2DVD data in order to classify into 8 hydrometeor classes the dominant type of precipitation during time intervals Δt. Aggregation over time intervals is conducted to reduce the computational cost, that may be excessive if each particle is individually considered and a relatively short Δt of 60 s is chosen to minimize the effect of mixing between separate hydrometeor types. 2DVD individual images are summarized over Δt with a high dimensional set of numerical features, constituting the necessary input for the SVM classifier. Data collected in the Swiss Alps, in the French Jura and in the Ontario region of Canada are used to train and validate the model.

The manuscript is structured as follows. Section 2 describes the experimental set up and the basic 2DVD data. Section 3 presents the hydrometeor classification model. Section 4 presents the main results and their quality assessment, while Sect. 5

AMTD
7, 1603–1644, 2014

provides examples of the outputs of the hydrometeor classification. Section 6 concludes the paper and lists some future perspectives.

2 Dataset description

2.1 Experiment locations

The 2DVD data employed in the experiments were collected during three field campaigns, between September 2009 and March 2013. The first campaign took place from September 2009, until June 2011 in Davos (CH): the 2DVD was deployed in the Swiss Alps, at an altitude of about 2500 m a.s.l. Data for a total of 1700 h of precipitation in liquid, mixed phase and solid precipitation were collected during this time frame. The second campaign took place in Remoray (FR), from December 2012 until March 2013, at an altitude of about 920 m in the context of an experiment focused on melting hydrometeors. 270 h of precipitation in solid, liquid and mixed phase were collected in this experiment. The third complementary campaign includes about 200 h of data (mainly solid precipitation) collected by three 2DVD instruments between December 2011 and March 2012 in the framework of the Global Precipitation Measurement mission (GPM, http://pmm.nasa.gov/precipitation-measurement-missions), in the Cold-season Precipitation Experiment (GCPEx) that took place in Ontario (CA).

2.2 2DVD instrument and data pre processing

The 2DVD working principle has been extensively described in Kruger and Krajewski (2002). Here we briefly summarize the most relevant features of the instrument. Figure 1 illustrates the 2DVD measurement principle (see Fig. 3 of Kruger and Krajewski, 2002, for more details).

Two orthogonal light sources coupled with two (A and B) line scanning cameras, generate two stacked measurement planes of about 10 cm × 10 cm. The planes are

AMTD
7, 1603–1644, 2014

vertically separated by a distance in the range of 6.2–7 mm (the exact value is determined by mechanical calibration). The cameras capture the falling particles at a resolution of 512 pixels (0.2 mm) at 34 kHz, and the planar distance between A and B measurements allows to infer the falling velocity.

The raw images need to be processed before being employed. This involves the filtering of unreasonable measurements, and the rematching of the measurements taken from camera A and B, in order to ensure that both images actually refer to the same particle. Filtering and rematching of 2DVD images is based on the work of Hanesch (1999) and Huang et al. (2010). We followed their workflows with a noteworthy modification. Among the filtering criteria, the authors (who were interested in snowfall only) were setting a maximum acceptable falling velocity of 4 ms^{-1} and 6 ms^{-1}, respecitvely. We increased this upper boundary to 14 ms^{-1}, large enough to include with sufficient margins the range of variation of rain (e.g., Beard, 1976) as well as large graupel (List and Schemena, 1971).

Despite this filtering, some non realistic particles can still be observed in the output. These particles appear as large objects, vertically oriented and elongated, as shown in Fig. 2. Because of these peculiarities, they are easily identified and excluded from the analysis presented in this paper.

An additional potential source of uncertainty (whose magnitude is currently not known in snowfall) is the image distortion that can occur when the horizontal component of the falling velocity of the particles is significant. This effect can be corrected in rainfall only, and further research (beyond the scope of this paper) is needed to develop correction schemes for snowfall measurements.

2.3 From single particles to global features

Couples of 2DVD A-B images are available for each particle falling in the measurement area. For the purpose of the present work, it is useful to summarize this large amount of information by choosing a set of relevant descriptors. Then, the statistical distribution of these descriptors in a time step Δt is used as input information for the hydrometeor

AMTD
7, 1603–1644, 2014

classification. The descriptors chosen in this work are listed in Table 1, and can be divided in 3 groups.

2.3.1 Joint descriptors

Two descriptors are obtained by combining the views of cameras A and B. They are: particle falling velocity v [ms^{-1}], and equivolumetric diameter D_e [mm]. D_e denotes the diameter of a sphere having the same volume of the falling particle. This descriptor was originally developed for raindrops, for which volumes can be calculated rather accurately from the 2-D views, and it can be extended to particles of any shape (Huang et al., 2010) as a reference measure of particle size.

2.3.2 Particle size

Other descriptors can be computed separately for camera A and camera B and Fig. 3 illustrates some of them. The apparent shaded areas $A_{A,B}$ and perimeters $P_{A,B}$ are readily available from the 2DVD measurements, while thicknesses $T_{A,B}$ and widths $W_{A,B}$ of each particle are defined with respect to a bounding box around the particle (Fig. 3). v, D_e, A, P, T and W together describe the particle bulk dimension and velocity.

2.3.3 Particle shape

Additional descriptors are computed to better characterize particle shape. They are adaptations to 2DVD images of dimensionless shape metrics commonly used in the analysis of land-cover images for remote sensing (Jiao and Liu, 2012):

$$\mathrm{PF}_{A,B} = \frac{A_{A,B}}{A^r_{A,B}} \quad (0,1] \tag{1}$$

$$\mathrm{FORM}_{A,B} = \frac{4\pi A_{A,B}}{P^2_{A,B}} \quad (0,1] \tag{2}$$

AMTD
7, 1603–1644, 2014

$$\mathrm{SqP}_{\mathrm{A,B}} = 1 - 4\frac{\sqrt{A_{\mathrm{A,B}}}}{P_{\mathrm{A,B}}} \quad [1 - 2/\sqrt{\pi}, 1) \tag{3}$$

$$\mathrm{FD}_{\mathrm{A,B}} = 2\frac{\ln(P_{\mathrm{A,B}}/4)}{\ln(A_{\mathrm{A,B}})} \quad [1, 2] \tag{4}$$

$$\mathrm{SI}_{\mathrm{A,B}} = \frac{P_{\mathrm{A,B}}}{4\sqrt{A_{\mathrm{A,B}}}} \quad [\sqrt{\pi}/2, +\infty] \tag{5}$$

$$\mathrm{ELONG}_{\mathrm{A,B}} = \frac{W_{\mathrm{A,B}}}{T_{\mathrm{A,B}}} \quad [1, +\infty] \tag{6}$$

$$\mathrm{ROUND}_{\mathrm{A,B}} = 4\frac{A_{\mathrm{A,B}}}{\pi {W_{\mathrm{A,B}}}^2} \quad (0, 1] \tag{7}$$

where $A^r_{\mathrm{A,B}}$ [mm^2] is the area of the bounding box calculated for image A (or B). $\mathrm{PF}_{\mathrm{A,B}}$ is called pixel fraction and compares the shaded area with the area of the bounding box. $\mathrm{PF}_{\mathrm{A,B}}$ is an index of compactness, as well as the roundness index, ($\mathrm{ROUND}_{\mathrm{A,B}}$) that compares the shaded area with a circular approximation. $\mathrm{FORM}_{\mathrm{A,B}}$ and square pixel metric $\mathrm{SqP}_{\mathrm{A,B}}$ are shape complexity indices based on the area-to-perimeter ratio, (they increase with decreasing complexity), while fractal dimension $\mathrm{FD}_{\mathrm{A,B}}$ and shape index $\mathrm{SI}_{a,b}$ are indeces based on the perimeter-to-area ratio (they increase with increasing complexity). $\mathrm{ELONG}_{\mathrm{A,B}}$ evaluates the degree of elongation of the particles.

As introduced above, the feature vector used in the SVM model refers to the distribution of descriptors in a time step Δt. Let us consider a time step Δt, during which N particles are recorded. We compute the mean, median, some quantiles (10 %, 25 %, 75 %, 90 %) and interquantiles (Q75–25, Q90–10) of each descriptor over the N particles available. Additionally, for the descriptors 3 to 13 of Table 1, we compute the correlation coefficient between the measurements of camera A and B. This leads to a set of 203 features calculated per time step: 16 deriving from camera combinations,

AMTD
7, 1603–1644, 2014

88 calculated separately for A and B (so 176 in total), and 11 correlation coefficients. We selected Δt to be 60 s, as a trade-off between representativeness and temporal resolution. Additionally, no statistics are computed if N is lower than 20 particles for a specific time step (Appendix A). The 88 features calculated separately for A and B have been verified to be consistent between each other, with biases generally lower than 10 %. This suggests that for these 88 features, the information carried by a single camera is sufficient. Therefore we can define, for each valid time step a final feature vector $\boldsymbol{x}$ containing 115 useful features, by using only the 88 single features from one of the two cameras.

3 Hydrometeor classification

This section details the proposed supervised classification approach. First we define the hydrometeor classes, then we detail how a training set is obtained and finally we present the classifier employed and its implementation to the available dataset.

3.1 Hydrometeor classes and training set

The principle of supervised classification methods is to use a set of N_{train} labeled observations (or training set) to train a classifier that will learn how to interpret new unlabeled observations. In our case, we need to assign the appropriate dominant hydrometeor type to a selected population of time steps Δt. The 2DVD offers the possibility to visualize the actual hydrometeor images, and the supervision is therefore conducted manually, according to the judgment of trained operators. The operators interpret the images by visualizing particle shapes, velocities, and taking into account the environmental conditions on site (time of the year, temperature). Additionally, for the data collected in Davos (CH), X-band radar observations over the region were available (e.g. Schneebeli et al., 2013), thus providing context information about the structure of precipitation, and in stratiform cases, about the altitude of the melting layer.

AMTD
7, 1603–1644, 2014

The visualization and pre-interpretation of a wide range of time steps led to the selection of 8 hydrometeor classes, to describe the possible precipitation types in the available dataset. Figure 4 shows an example of a typical particle belonging to each class. The classes are: Small particle-like (SP), Dendrite-like (D), Column-like (C), Graupel-like (G), Rimed particle-like (RIM), Aggregate-like (AG-l), Melting snow-like (MS-l), and Rain (R). The "-like" is added to emphasize that this approach identifies the dominant type of hydrometeor, which does not necessarily imply that: (i) there is only one type of hydrometeor in the considered time step, and (ii) that all hydrometeors exhibit the pristine shape and geometry.

The definition of some hydrometeor classes requires clarifications. SP time steps refer to particles falling during ice-phase precipitation that, given their size and the resolution of the instrument (0.2 mm), do not allow proper visual shape recognition. Small aggregates, as well as single ice crystals can be assumed to belong to this class. RIM is observed when riming processes smoothen the shapes of the hydrometeors and increase their fall speed, while G time steps refer to fully developed graupel, when the original shape of the rimed crystal is not recognizable anymore. MS is observed when the instrument records precipitation within the melting layer, and in these time steps raindrops, snowflakes, and smoother snowflakes with larger fall speed co-exist in mixed phase.

The creation of the training set involves the inspection of all the particles within each time step, in order to retrieve the dominant particle type and to provide the appropriate label. Particular attention is paid to the selection of time steps that are as pure as possible, for the subsequent training of the classifier. The training set employed in the present work includes $N_{\text{train}} = 400$ time steps, each of them numerically characterized by the 115 components of the associated feature vector $\boldsymbol{x}$ defined in Sect. 2.3.

AMTD
7, 1603–1644, 2014

3.2 Classification method

In this section, we present the classifier used, the SVM. Then, we will briefly detail an extension of SVM allowing to retrieve the importance of each input feature (or group of features) in the model, SVM-MKL.

3.2.1 SVM

Support Vector Machines (Boser et al., 1992; Scholkopf and Smola, 2001), also known as large margin classifier, are linear classifiers, which find the best linear separation between samples belonging to two classes. In our case, samples are time steps i of length Δt, represented by a vector $\boldsymbol{x}_i$ of $d = 115$ features and the classes are the 8 dominant types of hydrometeors, y_i. The model is trained on known couples $X_{\text{train}} = \{\boldsymbol{x}_i, y_i\}_{i=1}^{N_{\text{train}}}$, with $\boldsymbol{x}_i \in \mathbb{R}^d$ and $y_i \in [-1, 1]$. It must generalize well on a set of unknown samples, for which we do not know the dominant hydrometeor type $X_{\text{val}} = \{\boldsymbol{x}_v\}_{v=1}^{N_{\text{val}}}$.

SVM finds the best linear separation, of type $f(\boldsymbol{x}) = \langle \boldsymbol{w}, \boldsymbol{x} \rangle + b$, for which all training samples are at least at a distance of 1 from the separating plane. In other words, for all training samples $f(\boldsymbol{x})$ must be greater or equal to one. To differentiate between positive and negative examples, we also multiply this expression by 1 if the sample is of the positive class and by -1 if it is of the negative class (the two types of hydrometeors). Summing up, the constraint is $y_i(\langle \boldsymbol{w}, \boldsymbol{x}_i \rangle + b) \geq 1$, $\forall i \in N_{\text{train}}$. The strategy pursued by SVM (more details in Boser et al., 1992) is to find the separation which maximizes the distance between the closest points of each class, also called support vectors. This distance is called margin and is inversely proportional to the norm of the parameters vector, i.e. $\|\boldsymbol{w}\|^2$. In order to allow some classification errors, we also introduce a term ξ_i, which is non-zero for samples classified wrongly. The margin maximization problem is the following one:

AMTD
7, 1603–1644, 2014

$$\min_{\boldsymbol{w},b,\boldsymbol{\xi}} \left\{ \underbrace{\frac{1}{2}\|\boldsymbol{w}\|^2}_{\text{Complexity of the function}} + \underbrace{C\sum_{i=1}^{N_{\text{train}}} \xi_i}_{\text{Training errors}} \right\} \tag{8}$$

$$\text{s.t.} \begin{cases} y_i\left[\langle \boldsymbol{x}, \boldsymbol{w}\rangle + b\right] \geq 1 - \xi_i \\ \xi_i \geq 0 \quad \text{and} \quad i = 1, \ldots, N_{\text{train}} \end{cases}$$

C is a parameter that controls the constraint of perfect classification: if we allow some errors (by keeping C low), the margin becomes of larger width, thus reducing the dependence of the final model on training samples, that may be noisy or issued from errors in the measurements. A too high C increases drastically the value of the cost function, as soon as errors are made. In this case, the resulting model will achieve perfect classification of the training samples, but the risk of overfitting the training data and achieve poor generalization in the validation phase is higher.

This optimization model is solved using Lagrangian multipliers $\boldsymbol{\alpha}$, which allow to rewrite the problem as:

$$\max_{\boldsymbol{\alpha}} \left\{ \sum_{i=1}^{N_{\text{train}}} \alpha_i - \frac{1}{2}\sum_{i,j=1}^{N_{\text{train}}} \alpha_i \alpha_j y_i y_j \langle \boldsymbol{x}_i, \boldsymbol{x}_j \rangle \right\} \tag{9}$$

$$\text{s.t.} \quad 0 \leq \alpha_i \leq C \quad \text{and} \quad \sum_{i=1}^{N_{\text{train}}} \alpha_i y_i = 0$$

When the optimal solution to Eq. (9) is found (i.e., the vector of coefficients $\boldsymbol{\alpha}$), the label of an unknown sample $\boldsymbol{x}_v$ is assigned on the basis of the sign of the decision function, i.e., its position with respect to the hyperplane ($f(\boldsymbol{x}) = 0$):

$$y_v = \text{sign}\left(\sum_{i=1}^{N_{\text{train}}} \alpha_i y_i \langle \boldsymbol{x}_i, \boldsymbol{x}_v \rangle + b \right). \tag{10}$$

AMTD
7, 1603–1644, 2014

It can be observed that in the present formulation, SVM is only a binary classifier. A number of strategy exist to reduce multiclass to binary problems, and in the present work the one-against-one rule was employed (Hastie and Tibshirani, 1998).

3.2.2 Nonlinear SVM

SVM, as it has been presented above, can solve only linear problems (they define a linear hyperplane). However, there is an elegant solution to solve nonlinear problems. Let us go back to Eqs. (9) and (10): the solution of the optimization does not depend on the training samples themselves, but only one the dot products between samples (see $\langle \boldsymbol{x}_i, \boldsymbol{x}_j \rangle$ in Eq. 9). In the same way, the prediction for a new sample only depends on its dot products with the training samples (see $\langle \boldsymbol{x}_i, \boldsymbol{x}_v \rangle$ in Eq. 10). Dot products are measures of similarity between the samples. To perform nonlinear classification we need to find an estimate of their similarity in a projected space of higher dimension $\mathcal{H}$, where linear separation becomes possible[1]. To avoid defining explicitly the coordinates of the samples in the projected space, i.e., $\phi(\boldsymbol{x}_i)$, we can use functions that, even if expressed with points in the original space, correspond to dot products in the projected space $\mathcal{H}$: these functions are called kernels. Without entering mathematical details, that the interested reader can find in Scholkopf and Smola (2001), a kernel corresponds to a similarity function such that $K(\boldsymbol{x}_i, \boldsymbol{x}_j) = \langle \phi(\boldsymbol{x}_i), \phi(\boldsymbol{x}_j) \rangle$. This means that, for a given projection $\phi(\cdot)$, the kernel computed from $\boldsymbol{x}_i$ and $\boldsymbol{x}_j$ will correspond to their similarity in the space $\mathcal{H}$ defined by $\phi(\cdot)$. A classification, which is linear in the projected space, is nonlinear in the original space, as illustrated in Fig. 5.

In practice, in order to obtain a nonlinear classification with SVM, we replace the dot products in Eqs. (9) and (10) by kernel functions $K(\boldsymbol{x}_i, \boldsymbol{x}_j)$ and $K(\boldsymbol{x}_i, \boldsymbol{x}_v)$, respectively. A classical kernel to obtain such a behavior is the Radial Basis Function (RBF), which

[1]The Cover theorem states that the probability of linear separability increases with the dimensionality of the space (Cover, 1965).

AMTD
7, 1603–1644, 2014

is computed as follows:

$$K(\boldsymbol{x}_i, \boldsymbol{x}_j) = \exp\left(\frac{\|\boldsymbol{x}_i - \boldsymbol{x}_j\|^2}{2\sigma^2}\right). \quad (11)$$

The RBF kernel acts as a Gaussian similarity, which is maximal when considering the same samples ($K(\boldsymbol{x}_i, \boldsymbol{x}_i) = 1$), and decreases jointly with the decrease of similarity between the samples. The bandwidth σ controls the steepness of the Gaussian bell.

3.2.3 SVM-MKL

Even if very successful, SVM remains a black-box model, in the sense that no information about the importance of the initial variables can be retrieved from its results. All operations are optimized in the projected space $\mathcal{H}$: this means that, while it avoids to compute the projection of the samples explicitly, it also prevents to assess the importance of the different variables involved. Recent researches have offered a solution to this problem by introducing the concept of Multiple Kernel Learning (MKL, Rakotomamonjy et al., 2008).

SVM-MKL builds on the so-called Mercer conditions stating that a weighted sum of any positive definite function (a requirement for all kernel functions) is again definite positive (Mercer, 1909). This means that we can design a valid kernel by a linear combination of M base kernels $K_m(\boldsymbol{x}_i, \boldsymbol{x}_j)$, each one considering single timestep features (in this case $M = 115$) or sets of timestep features (in this case $M < 115$ and equals the number of groups of descriptors):

$$K(\boldsymbol{x}_i, \boldsymbol{x}_j) = \sum_{m=1}^{M} d_m K_m(\boldsymbol{x}_i, \boldsymbol{x}_j) \quad (12)$$

d_m is the weight attributed to each kernel K_m and is a measure of the importance of this kernel in the combination, i.e., of the variables composing it. It usually sums up

AMTD
7, 1603–1644, 2014

to 1. The SimpleMKL algorithm proposed in Rakotomamonjy et al. (2008) optimizes alternatively the weights and the SVM and allows to retrieve at the same time the relative importance of each group (d_m) and the SVM model associated to the final weighted combination.

In our experimentation, we used SimpleMKL to find the best combination of a series of RBF kernels K_m, each one assigned to a set of features referring to the same particle descriptor ($M = 13$, see Table 1). As an example, K_1 takes into account the 8 statistical features (Q10, Q25, Q50, Q75, Q90, IQ75–25, IQ90–10, mean) associated with the hydrometeor fall velocity v descriptor, while K_2 the 8 features associated with the equivolumetric diameter D_e, and so on.

4 Results and discussion

4.1 Performance-assessment metrics

The evaluation of the accuracy of classification is conducted via different metrics. The available N_{train} training observations are divided in two parts (N^*_{train} and N^*_{val}). N^*_{train} observations are used as training set to optimize the SVM parameters C and σ and to train the SVM, while the remaining N^*_{val} observations are kept for validation. A comparison is made between the SVM classification output $\{y^*_i\}_{i=1}^{N^*_{val}}$, and the true labels $\{y_i\}_{i=1}^{N^*_{val}}$ by evaluating a 8×8 confusion matrix **C**, as shown in Table 2. The elements $C(i,j)$ contain the number of observations classified in the i-th class, which in reality belong to the j-th class. The diagonal contains the correct classifications.

Given the confusion matrix, the global performances of the classifier are quantified by the overall accuracy (OA), and Cohen's Kappa (K):

$$\mathrm{OA} = \frac{\sum_{i=1}^{S} C(i,i)}{N} \times 100 \qquad (13)$$

AMTD
7, 1603–1644, 2014

$$\mathcal{K} = \frac{OA - P_{\text{est}}}{1 - P_{\text{est}}} \tag{14}$$

$$P_{\text{est}} = \frac{\sum_{i=1}^{S}\left(\sum_{j=1}^{S} C_{j,i} \sum_{j=1}^{S} C_{i,j}\right)}{N^2}$$

where S is the total number of classes, and N the total number of observations (in our case $S = 8$ and $N = N^*_{\text{val}}$). $\mathcal{K}$ takes into account the correct prediction that might occurs by chance, namely P_{est}, and is a robust metric in case of unbalanced classes.

Then, we look at the performances obtained within each class. For this purpose, we use:

$$\text{OA}_k = \frac{C(k,k)}{\sum_{i=1}^{S} C(k,i)} \times 100 \tag{15}$$

$$\text{POD}_k = \frac{C(k,k)}{\sum_{i=1}^{S} C(i,k)} \tag{16}$$

$$\text{POFD}_k = \frac{\left[\sum_{i=1}^{S} C(k,i)\right] - C(k,k)}{\sum_{i=1}^{S} C(k,i)} \tag{17}$$

where OA_k is the accuracy of the k-th class, POD_k and POFD_k are the associated probability of detection and false detection.

AMTD
7, 1603–1644, 2014

4.2 Evaluation of the quality of the training set

N_{train} observations are available in total as training set, and we must verify that this amount is sufficient for the present task. In other words we want to assess here if a larger N_{train} would improve significantly the hydrometeor classification. To do so we proceed as follows: (1): $N_{train} = 400$ is initially randomly split into $N^*_{train} = 300$ and $N^*_{val} = 100$; (2): N^*_{train} is iteratively reduced in size, while the orginal N^*_{val} is kept for validation; (3): Evaluation of the performances is conducted at each step; (4): steps (1)–(3) are repeated with 200 realizations of the original split.

Figure 6 shows the evolution of $\mathcal{K}$ as a function of the number of training samples in the training set (N^*_{train}). We can observe that N^*_{train} larger than 200 does not lead to significant improvements in terms of $\mathcal{K}$, while when N^*_{train} is smaller than 100, the performances start to degrade sharply. These results suggest that the total available labeled samples (400) are sufficient for the present classification task.

4.3 Evaluation of the classification performances

For validation purposes, we focus now on 200 realization of the case $N^*_{train} = 300$, $N^*_{val} = 100$. The classification achieves accurate global results, both in terms of OA and $\mathcal{K}$. As shown in Table 3, $\mathcal{K}$ and OA mean values are 0.88 and 89 %, and in 90 % of the cases they take values higher than 0.84 and 86 %, respectively. Additionally, $\mathcal{K}$ tends to be close to OA, indicating that the amount of correct classification occurring by chance is very limited.

The classification performance associated to each hydrometeor class is summarized in Fig. 7. It can be observed that all the hydrometeor classes are identified with median OA_k always greater than 84 %, POD_k greater than 0.84, and $POFD_k$ lower than 0.16. Overall, rainfall (R) hydrometeor class achieves the best scores, together with columns (C). R hydrometeors show a POD_k equal to one, meaning that errors for this class are uniquely false detections. On the contrary, C hydrometeors show $POFD_k$ and OA_k very close to one, and the errors for this class are due mainly to missed detection, with

AMTD
7, 1603–1644, 2014

POD_k scores around 0.9 in median. Graupel (G) is mostly affected by missed detections, and shows a relatively large interquantile spread for POD_k, around the median value of 0.84. Small particles (SP) have the highest false detection rate, with median $POFD_k$ close to 0.15. Dendritic snow (D) exhibits the largest interquantile spreads, around otherwise satisfactory median values of 86 % (OA_k), 0.89 (POD_k), and 0.14 ($POFD_k$), followed by rimed particles (RIM) that exhibit a similar behavior, achieving anyway higher scores for all the metrics. Aggregates (AG) and melting snow (MS) are both correctly predicted, with lower interquantile spread, median OA_k larger than 88 %, POD_k larger than 0.89 and $POFD_k$ lower than 0.12.

A last consideration concerns the choice of SVM as classifier. Other methods are used to solve similar tasks in various fields of the environmental sciences, for example linear discriminant analysis (LDA) or neural network (NN) (e.g., Goosaert and Alam, 2009; Robert et al., 2013). Comparison with these 2 methods showed that the proposed SVM scheme outperforms LDA by more than 0.2 and NN by more than 0.1 in terms of $\mathcal{K}$.

4.4 Ranking of descriptors

The SimpleMKL algorithm is applied to learn the most relevant descriptors in the classification process, as explained in Sect. 3.2.3. Referring to Eq. (12), it was observed that 5 groups of features out of the 13 ones (one per descriptor, each including the 8 or 9 statistical features extracted from its distribution in $\Delta t = 60$ s), were accounting for about 70 % (Fig. 8) of the total weights and therefore are considered hereafter as the most important ones. They are, in decreasing order of importance: pixel fraction PF, velocity v, equivolume diameter D_e, form index FORM and thickness T, with associated weights d_m of 0.193, 0.181, 0.13, 0.112 and 0.098, respectively. This does not imply that the remaining 8 descriptors are negligible in the classification process, but we expect to find a more immediate and intuitive physical meaning in these 5 top-ranked ones.

AMTD
7, 1603–1644, 2014

5 Application on unlabeled data

This section presents some examples of the classification output, on data not included in the training set of the algorithm, and collected during the measurement campaign of Davos (CH).

5.1 17 March 2011

A snowfall event occurring on the 17 March 2011 is presented in Fig. 9. The air temperature recorded on a nearby site was constantly below freezing ($\approx -5\,^{\circ}$C) through all the event duration and different ice-phase hydrometeors were identified in the time window shown here. Initially (07:00–09:00 UTC) precipitation is dominated by small particles (SP), followed by a phase of instability (09:00–10:00 UTC) characterized by sharp variations of the identified hydrometeor classes. In a second time (10:00–12:30 UTC), graupel (G) and larger rimed particles (RIM) are identified. Panels (b), (c), and (d) of Fig. 9 illustrate the behavior in time of the three top ranked particle descriptors, namely pixel fraction PF, equivolume diameter D_e and fall velocity v. PF is around 0.7, in median value during the whole event, indicating relatively high particle compactness. D_e is initially below 1 mm in median value (SP phase), and it increases to values between 1 and 2 mm in the second part of the event (G and RIM phases). v exhibits the same trends as D_e and it increases when rimed particles and grauple are dominant.

5.2 12 January 2011

A different situation is depicted in Fig. 10, relative to a snowfall event recorded on the 12 January 2011. In this case, for the time window shown (19:00–24:00 UTC), precipitation is dominated by aggregates (AG) and dendritic shaped snow (D, at the end of the event). By comparing the present case with the one shown in Fig. 9, we observe a wider range of variation of particle sizes, with D_e ranging between 0.5 mm and 8 mm (AG), sometimes higher than 2 mm in median value. Particle compactness

AMTD
7, 1603–1644, 2014

is lower, with PF below 0.7 in median through all the event, slightly lower for D than for AG. This is due to the higher geometrical complexity of aggregates and dendrites, in comparison with small particles and graupel. The velocity v does not exhibit peculiar trends, and it remains around values of 1 ms^{-1} in median.

5.3 5 August 2010

The precipitation event occurred on the 5 August 2010 (Fig. 11) illustrates well the transition between liquid-phase and ice-phase precipitation. In the first part of the event (05:00–07:45 UTC) air temperature is around 4 °C, and drops to 0 °C in a second part of the event (07:45–08:00 UTC). After 08:00 UTC the air temperature stabilizes again around 0 °C. These trends in temperature are reflected directly in the dominant hydrometeor types classified: initially rain (R), then melting-snow (MS), and finally aggregates (AG). Rain is here characterized by v ranging from 2 ms^{-1} to 5 ms^{-1} (light rain, as seen also in D_e), larger than the typical velocities of ice-phase hydrometeors, and very high compactness with PF around 0.9 in median. In the transition from R to MS and AG, a clear and relatively smooth trend is observed for the three descriptors shown: v decreases to median values around 1 ms^{-1}, the range of variation of D_e increases, and the median PF drops around 0.6 in the AG phase at the same time, as the geometrical complexity of falling hydrometeors increases.

In general terms, the transition between R, MS and AG is captured well in the large available dataset. Figure 12 shows the occurrence of classification of these three classes as a function of the temperature. R occurs always at positive temperatures, MS maximum occurrence is between 2 °C and 1 °C, and AG around 0 °C and −1 °C (in agreement with Hobbs et al., 1974).

AMTD
7, 1603–1644, 2014

6 Summary and conclusions

In this paper we presented a hydrometeor classification method based on the interpretation of 2DVD data. The classification, conducted with the SVM technique, uses as input the statistical behavior of a set of particle descriptors over time steps Δt of 60 s. The SVM is trained with 400 examples labeled by expert users, and outputs the dominant hydrometeor type within Δt. Additionally, an estimation of the relative descriptive importance of the input features is provided, of particular interest when higher-level information on the particle characteristics is required.

Discrimination is performed between 8 hydrometeor classes: small particle-like, dendrite-like, column-like, graupel-like, rimed particle-like, aggregate-like, melting snow-like, and rain. Evaluation of the classification performances is conducted both in global and class-specific terms. The classifier achieves accurate results, with median OA and $\mathcal{K}$ of 90 % and 0.88 respectively. All the classes are identified with specific accuracy higher than 84 % in median value.

Three classification examples together with the time evolution of the top-ranked particle descriptors were used to illustrate the typical classification products in pure snowfall events and in the transition between snowfall and rainfall. Global hydrometeor type behavior as well as small-scale fluctuations can be observed.

The proposed classification of hydrometeors provides a very interesting additional information to the primary 2DVD products, that can also help better understand the microphysical processes characterizing ice-phase precipitation events. This work has also the potential to be a starting point for ground-based quantitative evaluation of products coming from polarimetric weather radars, and it could be adapted and implemented in different particle imaging systems, either ground-based or airborne.

The choice of the SVM as classifier makes the method well balanced in terms of accuracy and computational cost, and adaptable to real time applications. The main limitation is that the current implementation provides bulk information over a given time step Δt, large enough to be statistically significant, but cannot provide estimation of

AMTD
7, 1603–1644, 2014

hydrometeor mixtures over Δt. Future work will focus on the development of a particle-by-particle classification, more challenging in terms of computational requirements, that can lead to explicit quantification of hydrometeor mixtures.

Appendix A

Minimum number of particles for a reliable classification

The proposed classification method employes as input a set of statistical features calculated over N particles, within a time step Δt. Thus, when N is small, sampling problems can affect the estimation of such statistics. We want to set a minimum $N_{\min}$, such that if $N > N_{\min}$ the classification output is reliable.

Figure A1a shows the contribution that time steps Δt for small N have with respect to the total amount of data available, both in term of total number of particles and in term of total number of time steps.

We can observe that time steps Δt with low N contribute negligibly to the total particle count, but significantly to the total count of available time steps. In other words, time steps with a low number of particles carry only a small part of the total precipitation, but they are observed frequently.

Figure A1b illustrates the classification performance achieved when $N < 60$. This is obtained by taking 57 random subsets of the available training set (with known labels), and using them as validation of the SVM algorithm trained previously. We can observe that for $N < 20$ the performances degrade sharply, and become more than 20 % lower than cases with $N > 60$. A threshold $N_{\min} = 20$ is therefore selected.

Acknowledgements. For the data from Switzerland we thankfully acknowledge the help of Nick Dawes, and many others at the WSL-Institute for Snow and Avalanche Research SLF.

The participation of Devis Tuia was financed through the Swiss National Science (SNF) project number: PZ00P2_136827.

AMTD
7, 1603–1644, 2014

For the data from Canada, we are thankful to Patrick Gatlin, Walt Petersen, Gwo-Jong Huang and David Hudak.

We finally thank Carine Berne for accepting various instruments in her garden for a whole winter.

References

Beard, K. V.: Terminal velocity and shape of cloud and precipitation drops aloft, J. Atmos. Sci., 33, 851–864, 1976. 1608

Boser, B., Guyon, I., and Vapnik, V.: A training algorithm for optimal margin classifiers, in: 5th ACM Workshop on Computational Learning Theory, Pittsburgh, USA, 144–152, 1992. 1606, 1613

Brandes, E. A., Ikeda, K., Zhang, G., Schonhuber, M., and Rasmussen, R. R.: A statistical and physical description of hydrometeor distributions in Colorado snowstorms using a video disdrometer, J. Appl. Meteorol. Clim., 46, 634–650, doi:10.1175/JAM2489.1, 2007. 1604

Camps-Valls, G. and Bruzzone, L.: Kernel-based methods for hyperspectral image classification, IEEE T. Geosci. Remote, 43, 1351–1362, doi:10.1109/TGRS.2005.846154, 2005. 1606

Camps-Valls, G. and Bruzzone, L. (Eds.): Kernel Methods for Remote Sensing Data Analysis, Wiley, 2009. 1606

Cao, Q., Zhang, G. F., Brandes, E., Schuur, T., Ryzhkov, A., and Ikeda, K.: Analysis of video disdrometer and polarimetric radar data to characterize rain microphysics in Oklahoma, J. Appl. Meteorol. Clim., 47, 2238–2255, doi:10.1175/2008JAMC1732.1, 2008. 1604

Chandrasekar, V., Keranen, R., Lim, S., and Moisseev, D.: Recent advances in classification of observations from dual polarization weather radars, Atmos. Res., 119, 97–111, doi:10.1016/j.atmosres.2011.08.014, 2013. 1605

Cover, T. M.: Geometrical and statistical properties of systems of linear inequalities with applications in pattern recognition, IEEE T. Electron., EC-14, 326–334, doi:10.1109/PGEC.1965.264137, 1965. 1615

Delanoe, J., Protat, A., Jourdan, O., Pelon, J., Papazzoni, M., Dupuy, R., Gayet, J. F., and Jouan, C.: Comparison of airborne in situ, airborne radar-lidar, and spaceborne radar-lidar retrievals of polar ice cloud properties sampled during the POLARCAT campaign, J. Atmos. Ocean. Tech., 30, 57–73, doi:10.1175/JTECH-D-11-00200.1, 2013. 1605

AMTD

7, 1603–1644, 2014

Dolan, B. and Rutledge, S. A.: A theory-based hydrometeor identification algorithm for X-band polarimetric radars, J. Atmos. Ocean. Tech., 26, 2071–2088, doi:10.1175/2009JTECHA1208.1, 2009. 1605

Elmore, K. L.: The NSSL hydrometeor classification algorithm in winter surface precipitation: evaluation and future development, Weather Forecast., 26, 756–765, doi:10.1175/WAF-D-10-05011.1, 2010. 1606

Feind, R. E.: Comparison of three classification methodologies for 2D probe hydrometeor images obtained from the armored T-28 aircraft, Tech. Rep. SDSMT/IAS/R08-01, Institute of Atmospheric Sciences, South Dakota School of Mines and Technology, Rapid City, SD, USA, 2008. 1605

Foresti, L., Tuia, D., Kanevski, M., and Pozdnoukhov, A.: Learning wind fields with multiple kernels, Stoch. Env. Res. Risk A., 25, 51–66, doi:10.1007/s00477-010-0405-0, 2011. 1606

Goosaert, E. and Alam, R.: Ensemble classifier for winter storm precipitation in polarimetric radar data, in: Seventh conference on artificial intelligence and its applications to the environmental sciences, Phoenix, USA, 2009. 1620

Hanesch, M.: Fall velocity and shape of snowflakes, Ph.D. thesis, Swiss Federal Institute of Technology Zurich, 1999. 1608

Hastie, T. and Tibshirani, R.: Classification by pairwise coupling, Ann. Stat., 26, 451–471, 1998. 1615

Hobbs, P. V., Chang, S., and Locatelli, J. D.: The dimensions and aggregation of ice crystals in natural clouds, J. Geophys. Res., 79, 2199–2206, doi:10.1029/JC079i015p02199, 1974. 1622

Houze, R. A. J.: Cloud Dynamics, Academic Press, San Diego, 1993. 1605

Huang, G., Bringi, V. N., Cifelli, R., Hudak, D., and Petersen, W. A.: A methodology to derive radar reflectivity liquid equivalent snow rate relations using C-band radar and a 2D video disdrometer, J. Atmos. Ocean. Tech., 27, 637–651, 2010. 1604, 1608, 1609

Jiao, L. and Liu, Y.: Analyzing the shape characteristics of land use classes in remote sensing imagery, ISPRS Annals of Photogrammetry, Remote Sensing and Spatial Information Sciences, I-7, 135–140, doi:10.5194/isprsannals-I-7-135-2012, 2012. 1609

Kruger, A. and Krajewski, W. F.: Two-dimensional video disdrometer: a description, J. Atmos. Ocean. Tech., 19, 602–617, 2002. 1604, 1607

AMTD
7, 1603–1644, 2014

List, R. and Schemena, R.: Free-fall behavior of planar snow crystals, conical graupel and small hail, J. Atmos. Sci., 28, 110–115, doi:10.1175/1520-0469(1971)028<0110:FFBOPS>2.0.CO;2, 1971. 1608
Marzano, F. S., Cimini, D., and Montopoli, M.: Investigating precipitation microphysics using ground-based microwave remote sensors and disdrometer data, Atmos. Res., 97, 583–600, doi:10.1016/j.atmosres.2010.03.019, 2010. 1605
Mercer, J.: Functions of positive and negative type and their connection with the theory of integral equations, Philos. T. R. Soc., 209, 415–446, 1909. 1616
Rakotomamonjy, A., Bach, F., Canu, S., and Grandvalet, Y.: SimpleMKL, J. Mach. Learn. Res., 9, 2491–2521, 2008. 1606, 1616, 1617
Robert, S., Foresti, L., and Kanevski, M.: Spatial prediction of monthly wind speeds in complex terrain with adaptive general regression neural networks, Int. J. Climatol., 33, 1793–1804, doi:10.1002/joc.3550, 2013. 1620
Schneebeli, M., Dawes, N., Lehning, M., and Berne, A.: High-resolution vertical profiles of polarimetric X-band weather radar observables during snowfall in the Swiss Alps, J. Appl. Meteorol. Clim., 52, 378–394, doi:10.1175/JAMC-D-12-015.1, 2013. 1605, 1611
Scholkopf, B. and Smola, A. J.: Learning with Kernels: Support Vector Machines, Regularization, Optimization, and Beyond, MIT Press, Cambridge, MA, USA, 2001. 1613, 1615
Schuur, T. J., Ryzhkov, A. V., Zrnic, D. S., and Schonhuber, M.: Drop size distributions measured by a 2D video disdrometer: comparison with dual-polarization radar data, J. Appl. Meteorol., 40, 1019–1034, doi:10.1175/1520-0450(2001)040<1019:DSDMBA>2.0.CO;2, 2001. 1604
Straka, J. M., Zrnic, D. S., and Ryzhkov, A. V.: Bulk hydrometeor classification and quantification using polarimetric radar data: synthesis of relations, J. Appl. Meteorol., 39, 1341–1372, 2000. 1605
Sullivan, S.: Evaluation of support vector machines and minimax probability machines for weather prediction, in: Seventh conference on artificial intelligence and its applications to the environmental sciences, Phoenix, USA, 2009. 1606
Thurai, M. and Bringi, V. N.: Drop axis ratios from a 2D video disdrometer, J. Atmos. Ocean. Tech., 22, 966–978, doi:10.1175/JTECH1767.1, 2005. 1604
Thurai, M., Hudak, D., and Bringi, V. N.: On the possible use of copolar correlation coefficient for improving the drop size distribution estimates at C band, J. Atmos. Ocean. Tech., 25, 1873–1880, doi:10.1175/2008JTECHA1077.1, 2008. 1604

AMTD
7, 1603–1644, 2014

Thurai, M., Szakall, M., Bringi, V. N., Beard, K. V., Mitra, S. K., and Borrmann, S.: Drop shapes and axis ratio distributions: comparison between 2D video disdrometer and wind-tunnel measurements, J. Atmos. Ocean. Tech., 26, 1427–1432, doi:10.1175/2009JTECHA1244.1, 2009. 1604

Tuia, D., Camps-Valls, G., Matasci, G., and Kanevski, M.: Learning relevant image features with multiple-kernel classification, IEEE T. Geosci. Remote, 48, 3780–3791, doi:10.1109/TGRS.2010.2049496, 2010. 1606

Volpi, M., Tuia, D., Bovolo, F., Kanevski, M., and Bruzzone, L.: Supervised change detection in VHR images using contextual information and support vector machines, Int. J. Appl. Earth Obs., 20, 77–85, doi:10.1016/j.jag.2011.10.013, 2013. 1636

Xue, M., Droegemeier, K. K., and Wong, V.: The Advanced Regional Prediction System (ARPS); a multi-scale nonhydrostatic atmospheric simulation and prediction model– Part 1: Model dynamics and verification, Meteorol. Atmos. Phys., 75, 161–193, doi:10.1007/s007030070003, 2000. 1605

Yuter, S. E., Kingsmill, D. E., Nance, L. B., and Loeffler-Mang, M.: Observations of precipitation size and fall speed characteristics within coexisting rain and wet snow, J. Appl. Meteorol. Clim., 45, 1450–1464, doi:10.1175/JAM2406.1, 2006. 1605

Zeng, J. and Qiao, W.: Support vector machine-based short-term wind power forecasting, in: Power Systems Conference and Exposition (PSCE), 2011IEEE/PES, Phoenix, AZ, 20–23 March 2011, 1–8, doi:10.1109/PSCE.2011.5772573, 2011. 1606

Zhang, G., Xue, M., Cao, Q., and Dawson, D.: Diagnosing the intercept parameter for exponential raindrop size distribution based on video disdrometer observations: model development, J. Appl. Meteorol. Clim., 47, 2983–2992, doi:10.1175/2008JAMC1876.1, 2008. 1604

Zhang, G., Luchs, S., Ryzhkov, A., Xue, M., Ryzhkova, L., and Cao, Q.: Winter precipitation microphysics characterized by polarimetric radar and video disdrometer observations in central oklahoma, J. Appl. Meteorol. Clim., 50, 1558–1570, doi:10.1175/2011JAMC2343.1, 2011. 1604, 1605

AMTD
7, 1603–1644, 2014

Table 1. List of descriptors chosen to describe the particles recorded. Descriptors 1 to 2 come from combination of camera A and B; 3 to 6 describe particle size; 7 to 13 particle shape.

	Symbol	Full name	Units
1	v	fall velocity	[ms^{-1}]
2	D_e	equivolumetric diameter	[mm]
3	$A_{A,B}$	shaded area	[mm^2]
4	$P_{A,B}$	shaded perimeter	[mm]
5	$T_{A,B}$	particle thickness	[mm]
6	$W_{A,B}$	particle width	[mm]
7	$PF_{A,B}$	pixel fraction	[–]
8	$FORM_{A,B}$	form index	[–]
9	$SqP_{A,B}$	square pixel metric	[–]
10	$FD_{A,B}$	fractal dimension	[–]
11	$SI_{A,B}$	shape index	[–]
12	$ELONG_{A,B}$	elongation	[–]
13	$ROUND_{A,B}$	roundness	[–]

AMTD
7, 1603–1644, 2014

Table 2. Example of a confusion matrix obtained during validation of the SVM calssification for a validation set N^*_{val} of 100 observations. Correct classifications are situated on the diagonal, and misclassifications are in the off-diagonal entries.

		True							
		SP	D	C	G	RIM	AG	MS	R
Predicted	SP	**14**	0	1	3	0	0	0	0
	D	0	**9**	0	0	0	3	0	0
	C	0	0	**9**	0	0	0	0	0
	G	1	0	0	**9**	0	0	0	0
	RIM	0	0	0	0	**8**	0	0	0
	AG	0	0	0	0	0	**11**	1	0
	MS	0	0	0	2	0	1	**13**	0
	R	0	0	0	0	0	0	0	**15**

AMTD
7, 1603–1644, 2014

Table 3. Mean values and relevant quantiles of $\mathcal{K}$ [–] and OA [%], calculated over 200 iterations of the SVM validation procedure.

Parameter	Q10	Q25	Q50	Q75	Q90	mean
$\mathcal{K}$	0.84	0.86	0.88	0.91	0.93	0.88
OA	86	88	90	92	94	89

AMTD
7, 1603–1644, 2014

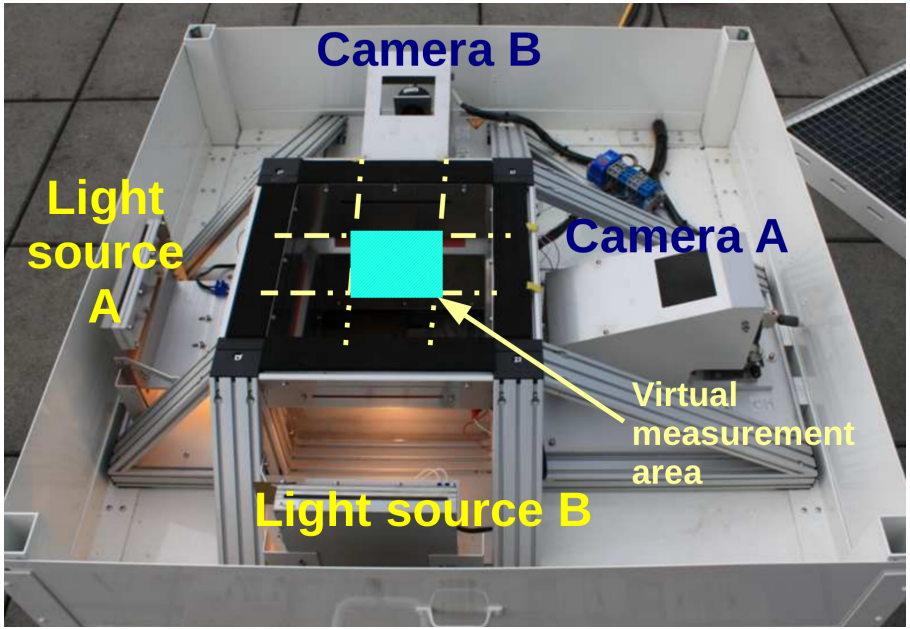

Fig. 1. 2DVD measurement principle.

AMTD
7, 1603–1644, 2014

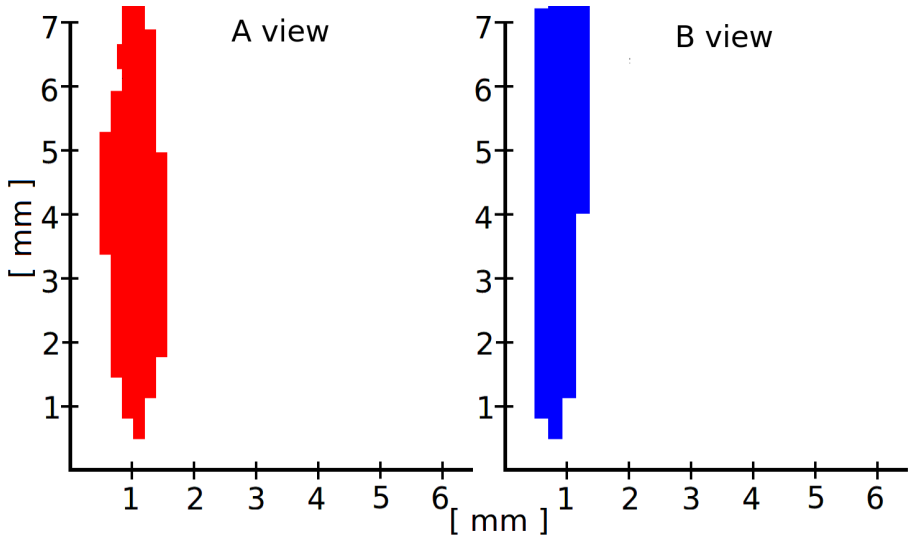

Fig. 2. Example of A-B views of a non-realistic particle, that needs to be filtered.

AMTD
7, 1603–1644, 2014

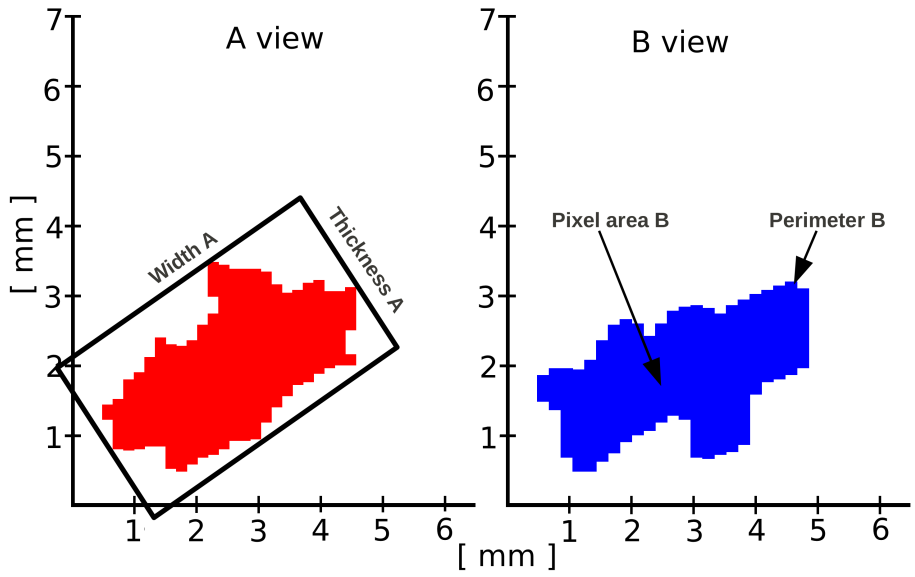

Fig. 3. Examples of particles descriptors of 2DVD images (camera A and B). On camera A: width (W_A [mm]) and thickness (T_A [mm]) of the bounding box enclosing the particle. On camera B: particle apparent perimeter (P_A [mm]) and shaded area (A_A [mm^2]).

AMTD
7, 1603–1644, 2014

Hydrometor classification from 2-D videodisdrometer data

J. Grazioli et al.

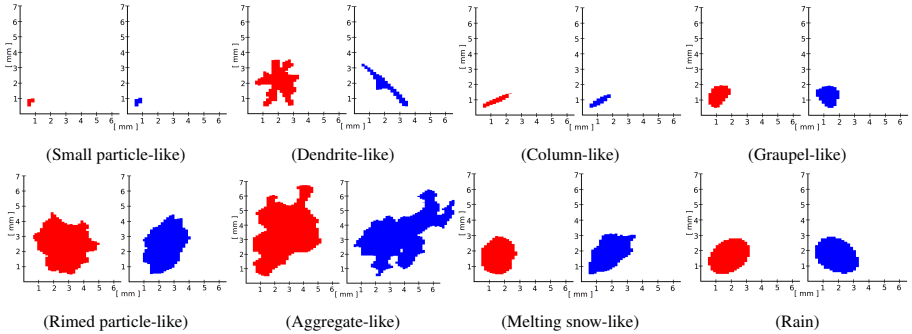

Fig. 4. Examples of particle images (two camera views: A left, B right), belonging to time steps dominated by a particular hydrometeor class.

AMTD
7, 1603–1644, 2014

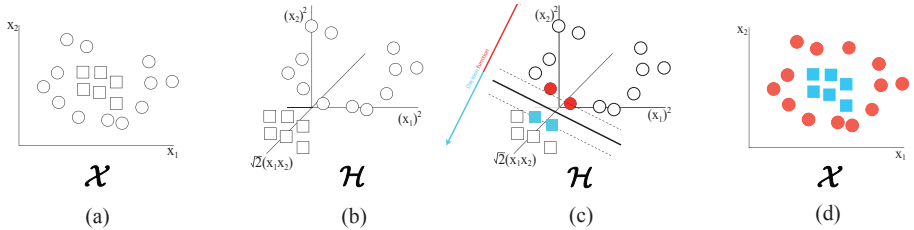

Fig. 5. Illustration of nonlinear SVM. **(a)** A nonlinearly separable dataset in the input space $\mathcal{X}$, involving two classes (squares and circles). **(b)** Projection on a 3D space $\mathcal{H}$ by the kernel $K(\boldsymbol{x}_i, \boldsymbol{x}_j) = \langle \boldsymbol{x}_i, \boldsymbol{x}_j \rangle^2$. **(c)** Linear classification in the projected space $\mathcal{H}$ (filled dots are support vectors). **(d)** Corresponding nonlinear decision function in the original space $\mathcal{X}$. Adapted from Volpi et al. (2013).

AMTD
7, 1603–1644, 2014

Hydrometor classification from 2-D videodisdrometer data

J. Grazioli et al.

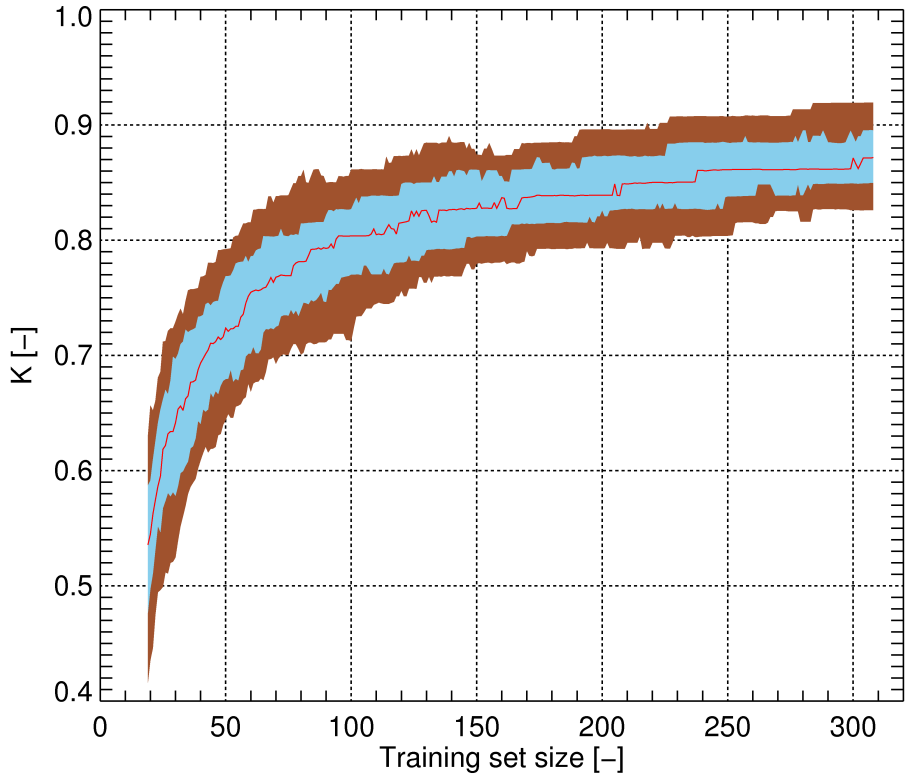

Fig. 6. Evolution of $\mathcal{K}$ [–], as a function of the training set size. The solid red line indicates the median, while the blue and brown areas represent Q75–25 and Q90–10, respectively. The size of the training set has been varied with a step of 1, between 300 and 20. Statistics are based on 200 realizations.

AMTD
7, 1603–1644, 2014

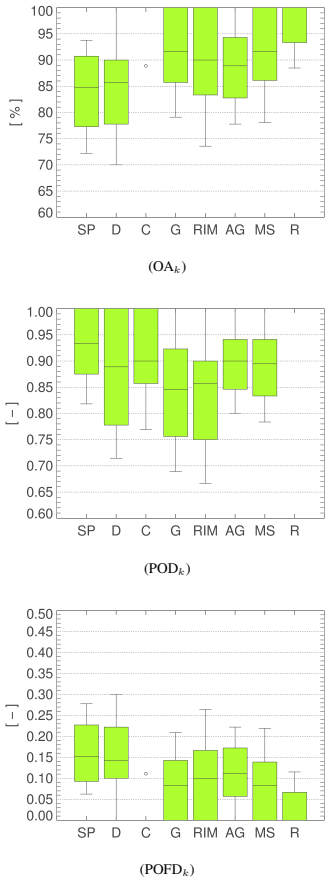

Fig. 7. Barplots of: OA_k [%], POD_k [–], $POFD_k$ [–] associated with the 8 hydrometeor classes undergoing classification. Statistics calculated over 200 realizations of the SVM validation. Single points (outliers) are represented as circles.

AMTD
7, 1603–1644, 2014

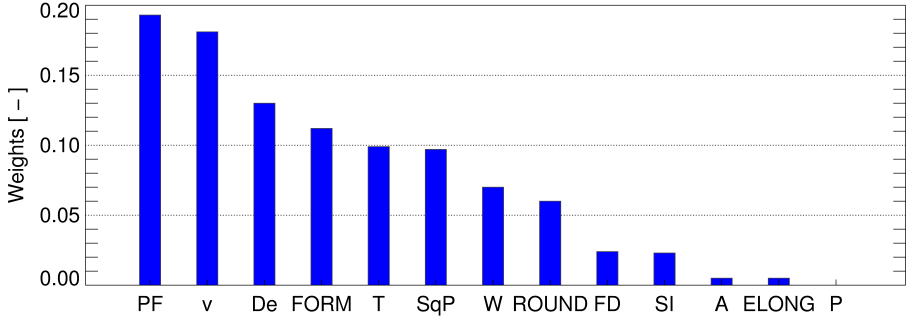

Fig. 8. Weights d_m of the 13 K_m Kernels, associated with the 13 particle descriptors used in the present study.

AMTD
7, 1603–1644, 2014

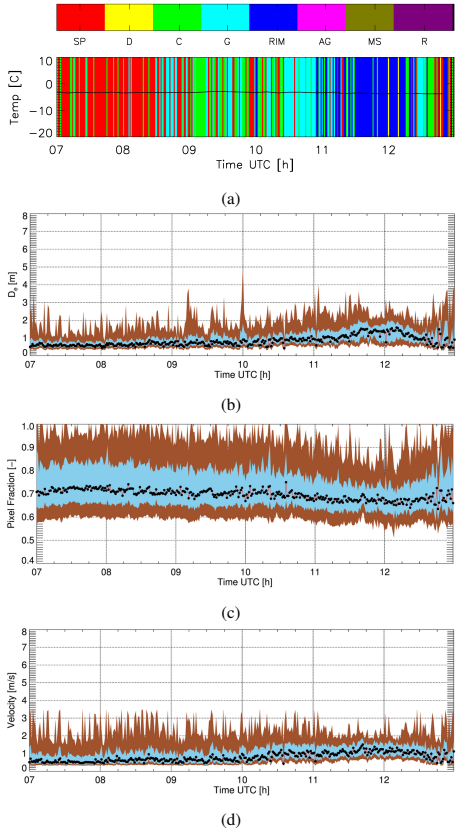

Fig. 9. Snowfall event recorded the 17 March 2011. Time series of: **(a)** dominant hydrometeor type as classified with the SVM and local ambient temperature [°C], as measured by a closely located weather station, **(b)** D_e [mm], **(c)** pixel fraction of camera A PF_A [–], **(d)** fall velocity v [$m\,s^{-1}$]. In panels **(b)**, **(c)**, and **(d)** black dots connected by the red solid line indicate the median value, while the shaded areas depict Q90–10 and Q75–25, respectively.

AMTD
7, 1603–1644, 2014

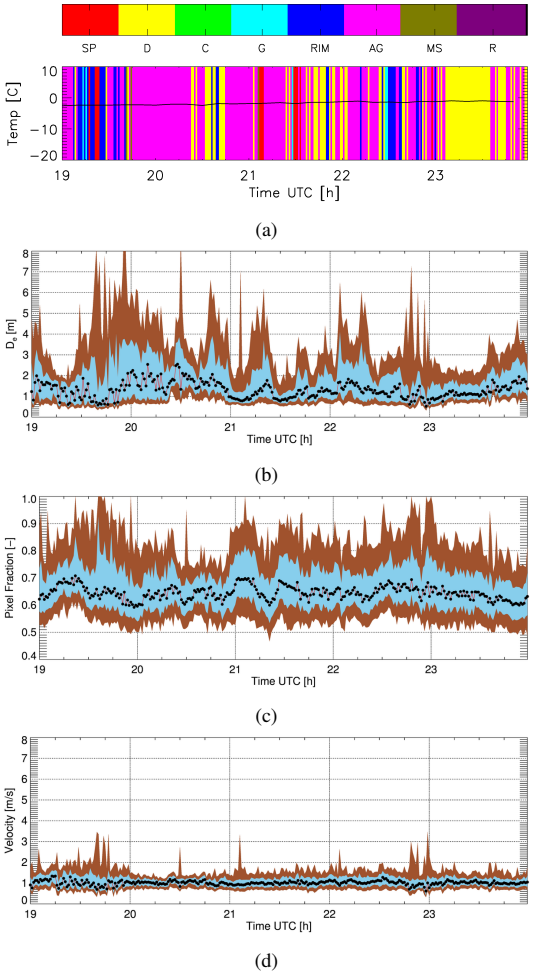

Fig. 10. As in Fig. 9, for the 12 January 2011.

AMTD
7, 1603–1644, 2014

Hydrometor classification from 2-D videodisdrometer data

J. Grazioli et al.

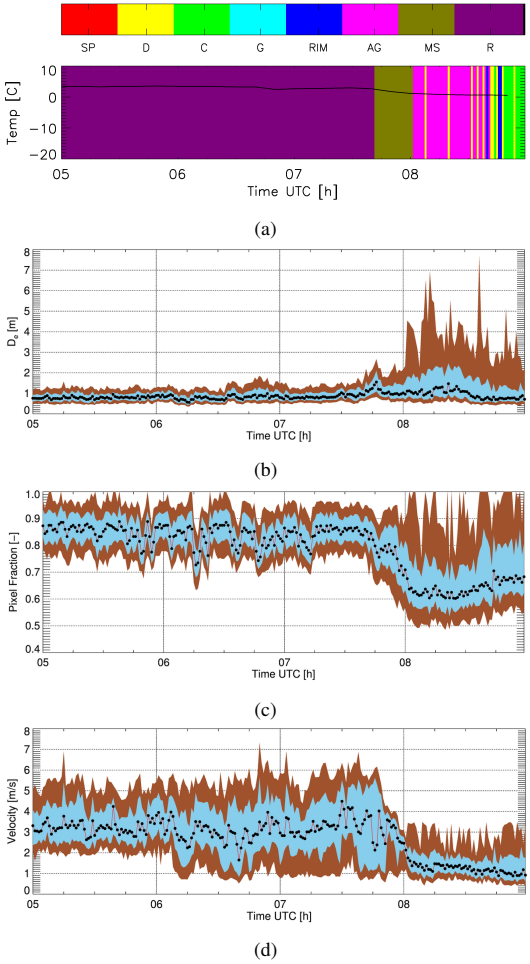

Fig. 11. As in Fig. 9, for the 5 August 2010.

AMTD
7, 1603–1644, 2014

Hydrometor classification from 2-D videodisdrometer data

J. Grazioli et al.

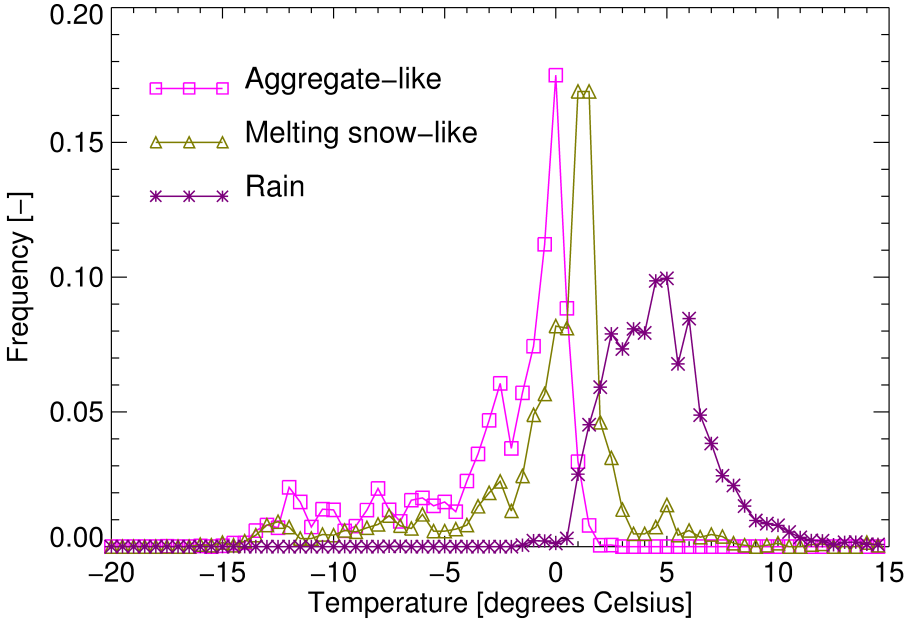

Fig. 12. Distribution of the occurrence of AG, MS and R as a function of air temperature. The distribution is obtained by aggregation of all the 2DVD measurements collected during the field experiments of Davos 2009–2011 (CH) and Remoray 2012–2013 (FR), and temperature data are given by closely-located weather stations.

AMTD
7, 1603–1644, 2014

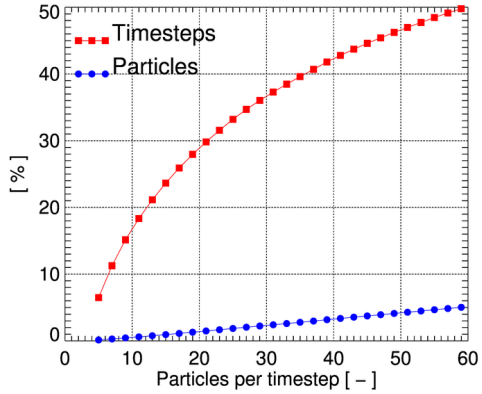

(a)

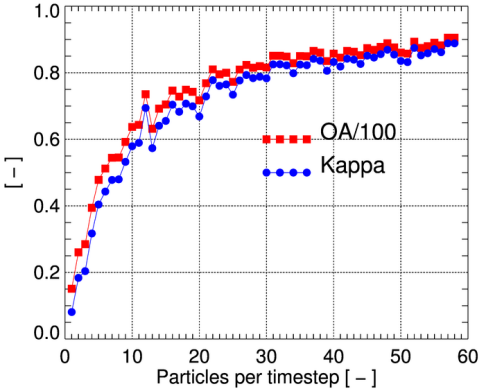

(b)

Fig. A1. (a) Contributions [%] of time steps Δt with less than 60 particles to the total database of observations. **(b)** Classification peformance as a function of the number of particles recorded per time step. Δt with less than 3 particles do not contribute to these statistics.

AMTD
7, 1603–1644, 2014